Insights into exhumation and mantle hydration processes at the Deep Galicia margin from a 3D high-resolution seismic velocity model

Bhargav Boddupalli[1*], Tim A. Minshull[1], Gaye Bayrakci[2], Gaël Lymer[3], Dirk Kläschen[4] and Tim J. Reston[5]

[1]School of Ocean and Earth Science, University of Southampton, UK.

[2]National Oceanography Centre, Southampton, UK.

[3]School of Earth Sciences, University College Dublin, Ireland.

[4]GEOMAR, Helmholtz Centre for Ocean Research Kiel, Germany.

[5]School of Geography, Earth and Environmental Sciences, University of Birmingham, UK.

Abstract

High-resolution velocity models developed using full waveform inversion (FWI) are capable of imaging fine details of the nature and structure of the subsurface. Using a 3D FWI velocity model of hyper-thinned crust at the Deep Galicia Margin (DGM), we constrain the nature of the crust at this margin by comparing its velocity structure with those in other similar tectonic settings. Velocities representative of both the upper and lower continental crust are present in this hyper-thinned crust. However, unlike in many other rifted margin settings, there is no clear evidence for distinct upper and lower crustal layers within the hyperextended crust. Our velocity model also shows evidence for exhumation of the lower crust under the footwalls of fault blocks to accommodate the extension. We used our model to generate a serpentinization map for the uppermost mantle at the DGM, at a depth of 100 ms (~340m) below the S-reflector, a low-angle detachment that marks the base of the crust at this margin. Based on this map, we propose that serpentinization began during rifting and continued into a post-rift phase until the faults were sealed. We find a weak correlation between the fault heaves and the degree of serpentinization beneath the hanging-wall blocks, indicating that serpentinization was controlled by a complex crosscutting and unrecognized faulting during and after rifting. A good match between topographic highs of S and local highly serpentinized areas of mantle suggests that the serpentinization process resulted in variable uplift of the S-surface.

* Now at the Institute for Geophysics, University of Texas at Austin, USA.

Plain Language Summary:

High-resolution P-wave velocities of the rocks of the extremely thinned crust at the Deep Galicia Margin (DGM) was used to understand the nature of the crust at this margin by comparing the rock velocities with those in other similar tectonic settings. Velocities representative of both the upper and lower continental crust are present in this thinned crust. Our velocity model shows that lower crustal rocks exhumed below the faults that cut through the entire crust reaching the mantle to accommodate the extension during rifting. We used our model

to generate a serpentinization map for the uppermost mantle at the DGM, at a depth of ~340m below the base of the crust at this margin. Based on this map, we propose that serpentinization began during rifting and continued after the fault motion stopped until the faults were sealed. We find a weak correlation between the fault heaves and the degree of serpentinization on the hanging wall side of the faults, indicating that serpentinization was controlled by a complex crosscutting fault network. A good match between topographic highs of the upper mantle surface and highly serpentinized areas of mantle suggests that the serpentinization process resulted in uplift of the mantle surface.

Main points:

1. Exhumation of the lower crust under the footwall of the normal faults to accommodate extension during early extension phases.
2. Water transportation to the mantle commenced during rifting and continued post-rifting until the fault were sealed.
3. Serpentinization was controlled by a complex cross-cutting and unrecognized faulting during and after rifting.

1. Introduction

The rifting and breakup of the continents is a first-order tectonic process that results in the formation of new ocean basins and rifted margins. Significant spatial variations in the magnitude of extension, in the nature of the extended crust and in the degree of syn-rift magmatism arise along rifted margins. Accordingly, depending on the magmatic budget involved and identified in their distal zones, rifted margins are often termed as "magma-poor" and "magma-rich" (e.g. Franke, 2013), with a wide range of structures between these two end-members. The distal zones of magma-poor margins are commonly characterized by hyperextended crust associated with a complex network of extensional faults and with mantle exhumation preceding eventual continental breakup (Peron-Pinvidic et al. 2013). The mechanisms involved in the final stages of rifting are among the most debated aspects of rifting processes. A range of mechanisms has been proposed to explain the development and evolution of crustal hyperextension before continental breakup, including the role and kinematics of faulting and detachment faults, the development of asymmetry, and the nature and rheology of the crust and mantle (Brune et al. 2014; Ranero & Pérez-Gussinyé, 2010; Reston, 2005; Reston, 2009). It has been proposed that during the final stages of extension, embrittlement of the lower crust occurs progressively as the crust thins until the upper and lower crust become coupled and entirely brittle (Perez-Gussinye and Reston, 2001). Hyperextension is then accommodated by large normal faults that cut through the entire brittle crust and sole out on the underlying top mantle (de Charpal et al. 1978; Lymer et al. 2019; Pérez-Gussinyé & Reston, 2001; Reston et al. 1996, 2007; Sibuet, 1992), with the normal faults acting as fluid conduits, transporting seawater to the upper mantle and resulting in its partial serpentinization (Bayrakci et al. 2016; Pérez-Gussinyé & Reston, 2001).

The Galicia Margin, west of Spain, is a sediment-starved, salt-free and magma-poor margin that has been studied extensively to understand the tectonics involved in the rifting process (e.g. Boillot & Winterer, 1988; Lymer et al. 2019). Extreme thinning of the continental crust towards zero thickness, reduced mantle velocities below the thinned crust and exhumed mantle, in the form of a Peridotite Ridge (PR) locally outcropping at the seafloor, were all first observed at the Galicia margin (Boillot et al. 1980; Boillot & Winterer, 1988). Seismic imaging of the hyperextended zone of the Galicia Margin, known as the Deep Galicia Margin (DGM), has revealed steeply dipping normal faults and tilted fault blocks overlying a band of discontinuous reflections collectively called the S-reflector (de Charpal et al. 1978; Boillot & Winterer, 1988; Reston et al. 1996, 2007). The lithosphere extension in the DGM was accommodated by a complex pattern of faulting resulting in the development of extremely thinned crust ($<$ 5km) before the eventual breakup seawards (Pérez-Gussinyé & Reston, 2001). Three main models of continental break-up have been proposed to explain crustal hyperextension in the DGM: polyphase faulting (Reston, 2005), sequential faulting (Ranero & Pérez-Gussinyé, 2010) and faulting by rolling hinge (Buck, 1988; Reston et al. 2007). In the polyphase faulting model, the fault blocks bounded by the normal faults are proposed to be rotated to low angles until the faults get locked up and new faults develop, preferentially cutting through the already existing faults and fault blocks overwriting the previous generation faults (Reston, 2005, 2007; Reston & McDermott, 2014). In the sequential faulting model, a new fault develops through the thinned crust seawards of the previously formed fault only when the latter has locked up. As a result, the locus of extension migrates toward the future rift centre, with only one fault active at a time (Ranero & Pérez-Gussinyé, 2010). The earlier rolling hinge model (Buck, 1988) is a form of sequential faulting in which the upper portion of a brittle fault flexes to low-angle to be abandoned, but continued slip on the steeper root zone results in the propagation from that root zone of a new shortcut fault through the hanging wall, so transferring a slice of that hanging wall to the footwall. The process repeats so that the rotated and abandoned segments of successive steep faults form a continuous sub-horizontal detachment surface (Buck, 1988; Reston et al. 2007). Based on the correlation between the heaves of the faults and the syn- and pre-rift packages observed on 3D seismic reflection images, Lymer et al. (2019) proposed that in the DGM, faulting moved progressively seaward as in the rolling hinge model, but with several linked faults active at a time instead of just one single fault.

One of the most intriguing questions is the evolution and role of the S-reflector in the tectonics of the DGM. S has been interpreted variously as the crust-mantle boundary, a brittle-ductile transition and a detachment fault (Ranero & Pérez-Gussinyé, 2010; Reston et al. 1996, 2007; Sibuet, 1992). Slip of the overlying crustal fault blocks above serpentinized mantle along the S-reflector is inferred to have resulted in intense fracturing and brecciation in the lower parts of the crust (Reston et al. 1996). In addition, a low-velocity zone of ~50 m thickness at the S-reflector level, comprising highly fractured serpentinized/crustal rocks, was

inferred from one-dimensional (1D) full waveform inversion (FWI) (Leythaeuser et al. 2005). 3D seismic reflection imaging has confirmed the presence of this "S-interval", interpreted as corresponding to fault rock material that thickens near intersections between the S-reflector and the overlying normal faults (Schuba et al. 2018).

In this paper, we interpret the seismic velocity model of the DGM that was derived from 3D FWI applied to ocean bottom seismic data by Boddupalli et al. (2021). Based on the velocity model, we discuss the nature of the crystalline crust at the DGM (Figure 1c) and present evidence for exhumation of the lower crust under the footwall of the normal faults. We also present a serpentinization map generated at a depth of 100 ms below the S-reflector and we compare this map with Schuba et al.'s (2019) map, that was obtained from a machine learning algorithm, trained with a velocity model from 2D FWI (Davy et al. 2018) and applied to the 3D reflection volume. Based on our serpentinization map, we propose that serpentinization of the mantle below the hyperextended crust commenced during the rifting but continued into the post-rift phase after slip of the fault blocks over the S-reflector had ceased.

1. Data and Method

Multichannel reflection and wide-angle seismic data were acquired at the DGM as part of the Galicia-3D (G3D) experiment. The seismic signals were generated by firing two airgun arrays comprising of 20 airguns each were fired alternately at an interval of ~37.5 m. The volume of the individual airgun array was 3,300 cu.in.. The multichannel seismic recording was carried out using four 6 km streamers with 200 m spacing and ocean bottom hydrophones/seismometers (OBS) were deployed at 80 locations within the 3D survey area to record simultaneously wide-angle seismic data (Figure 1). The multichannel seismic volume was 3D time-migrated over an area of 68.5 km (east-west) by 20 km (north-south). The wide-angle seismic data recorded by the OBSs were used to generate a high-resolution velocity model using 3D full waveform inversion (FWI) (Boddupalli et al. 2021). The dimensions of the FWI grid direction were 78.5 km in the east-west by 22.1 km in the north-south direction (Figure 1; Boddupalli et al. 2021). The starting model for this FWI was obtained by 3D traveltime tomography (Bayrakci et al. 2016). The 3D FWI model was validated by recovering anomalies introduced into the starting model performing synthetic tests and by overlaying the velocity model on 3D seismic images (Boddupalli et al. 2021). Our interpretations are limited to the regions where the anomaly recovery tests were able to recover the anomalies without smearing (Supplementary Figures 1 and 2). The maximum resolution of half a wavelength at 5.2 Hz (maximum frequency) corresponds to ~340 m for 3.5 km/s, ~580 m for 6 km/s and ~675 m for 7 km/s, but the resolution may vary depending on the data coverage. Further details of the data and FWI method are given by Boddupalli et al. (2021).

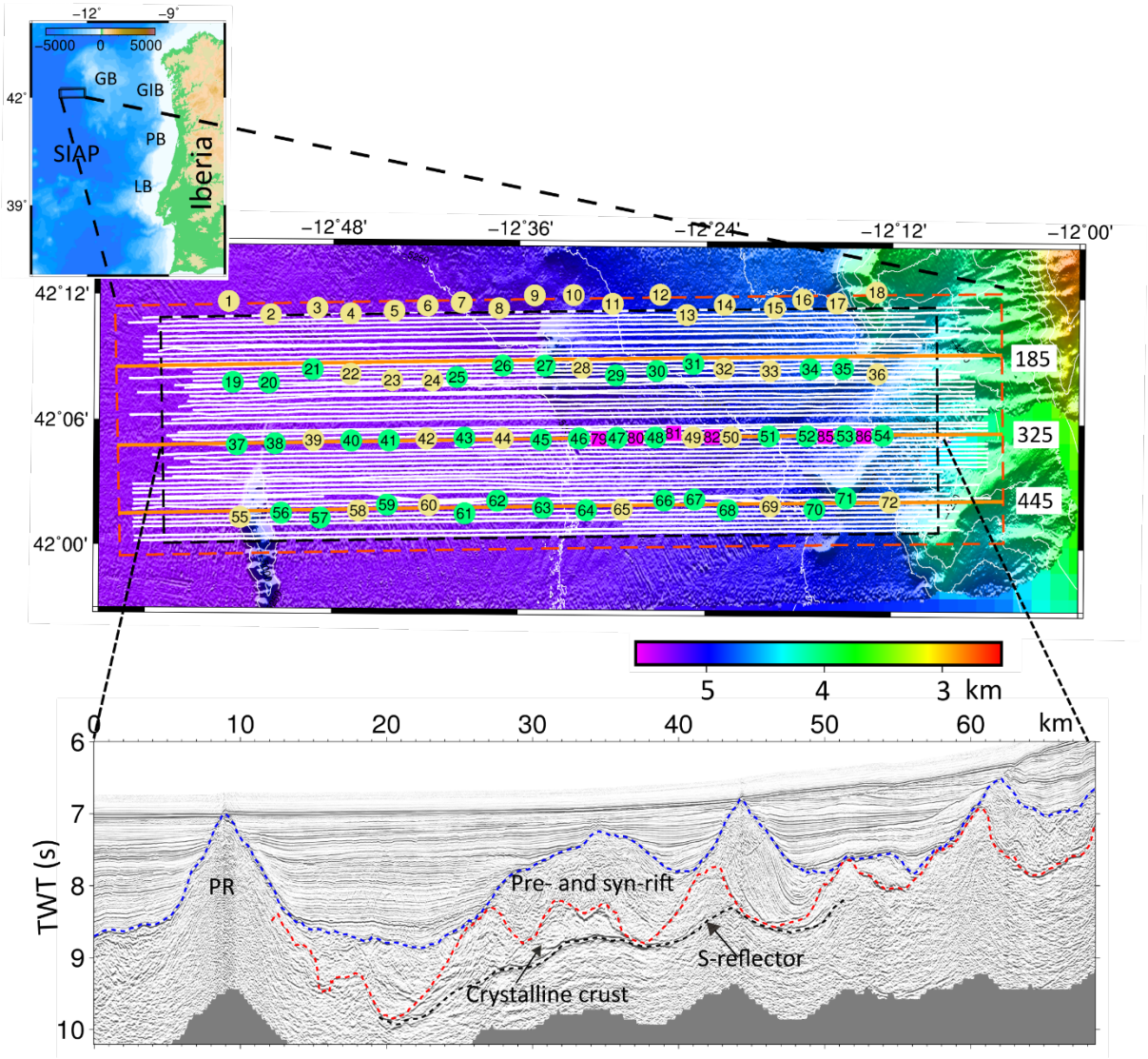

Figure 1 Bathymetric map of the DGM showing the location of the OBSs and seismic lines used in this study. The inset map shows the studied area (black box) west of Iberia. The dashed red box marks the area for the 3D FWI and the dashed black box marks the multichannel 3D seismic volume. The shot profiles recorded by the OBSs are shown in white lines. The orange numbered profiles mark the seismic-sections shown in Figures 6 and 7. Green circles mark OBS locations used for 3D FWI and yellow circle mark OBS locations that have not been used for FWI. The instruments in pink have only two shot profiles recorded directly above them and were used in full 3D FWI. GB, GIB, PB, LB and SIAP stand for Galicia Bank, Galicia Interior Basin, Porto Basin, Lusitanian

Basin and Southern Iberian Abyssal Plain, respectively. Profiles 185, 325 and 445 shown in orange correspond to 700, 420 and 180 sections in the 3D time migrated seismic volume (Lymer et al. 2019). Bottom figure is the 3D time-migrated section along profile 325 highlighting different geological sections in the DGM; PR stands for Peridotite Ridge.

1. **Results**

The top of the crystalline crust in the time-migrated and depth-converted multichannel seismic volume varies between ~4.3 km and 10.7 km depth, generally increasing westwards (Figure 2a). In the 3D FWI model, the velocities at the top of the crystalline crust lie between 1.5 and 5.7 km/s with a mean of 4.75 km/s and standard deviation of 0.95 km/s (Figure 2b). The top of the crystalline crust in a few locations almost reaches the seafloor, and the lower velocity limit is close to seawater velocity because of smoothing across the seafloor that used a 200 m window. These velocities show a similar pattern to the depth of the top of the crystalline crust, with lower velocities occurring where the top of the crystalline crust is shallower. We calculated the thickness of the crystalline crust by subtracting this depth from the depth of the S-reflector (Figure 2d). Crustal thickness varies between 0 and 3.6 km, with thickest crust near the summits of the faulted blocks (Figure 2d). The mean velocity of the crystalline crust in the FWI model is 6.01 km/s with a standard deviation of 0.44 km/s (Figure 2e). This velocity tends to decrease in the regions where the thickness of the crystalline crust increases.

We extracted velocities from the 3D FWI model at the S-reflector and below the S-reflector using the S-reflector two-way-times picked by Lymer et al. (2019) and converted to depth using the 3D FWI velocities (Figures 3 & 5 ; Boddupalli et al. 2021). The depth of the S-reflector varies between ~7 and ~12 km with deeper reflections in the south-west and shallow reflections in the south-east and central north (Figure 3a). We conducted an anomaly recovery test in which synthetic dataset generated using the FWI model was used as observed data and inverted using the same starting model as the FWI (Boddupalli et al. 2021; Zhao et al. 1992). The shapes of the anomalies were well recovered with little smearing, validating the anomalies introduced by 3D FWI (Boddupalli et al. 2021), but the amplitudes of the recovered anomalies are slightly lower than the actual anomalies (Supplementary Figure 1). Further validation of our velocity maps comes from a good match between the FWI model and multichannel seismic time slice at an average S time of 9s (Figure 4). The FWI model shows an abrupt lateral change in velocity that matches well the abrupt change in reflectivity that occurs at the S-reflector, indicating that the model has resolved well features at this depth (Figure 4). In the FWI model, the mean velocity at the S-reflector is 6.74 km/s with a standard deviation of 0.49 km/s, which is higher than but within error of the mean velocity in the tomographic model of 6.53 km/s (Bayrakci et al. 2016). The FWI has introduced finer-scale velocity variations at the S-reflector that match the topography of the S-reflector (Figure 3a & 3b). Such a correlation could arise from sampling along a rough surface

a smooth velocity model in which velocities increase with depth, but we rule out this origin because the correlation is much reduced in the starting model (Figure 3c). The minimum and maximum velocities at the S-reflector from the 3D FWI model are 4.9 km/s and 8.2 km/s, respectively.

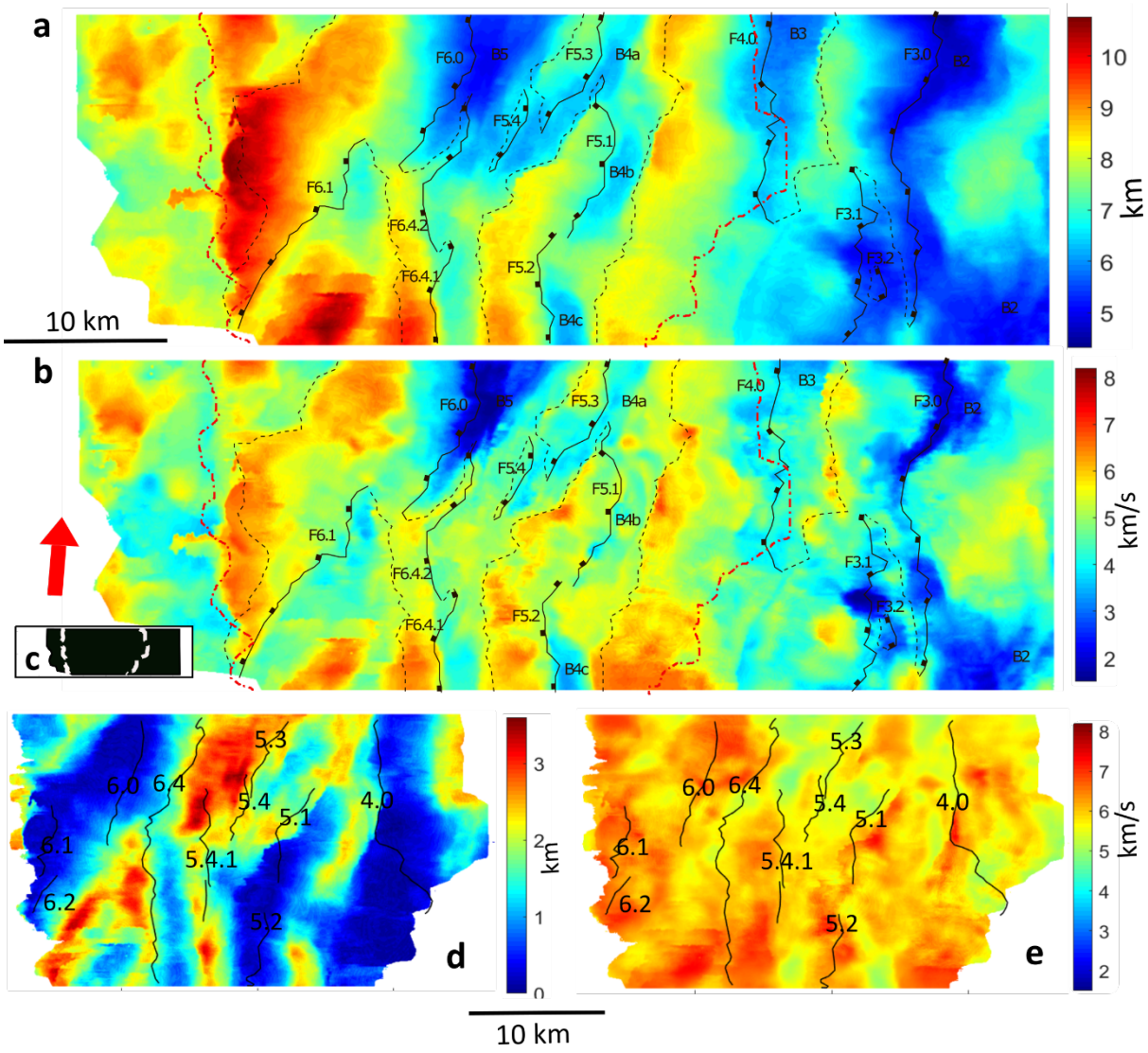

Figure 2 a) The top of the crystalline crust within the Galicia 3D volume (Lymer et al. 2019) converted to depth using the 3D FWI model (km) with faults (F-series) and fault blocks (B-series) numbered from Lymer et al. (2019). The footwall and hanging wall cut offs are marked as solid and dashed black lines, respectively. Dashed dotted red lines show the extent of the S reflector; b) velocities along the top of the crystalline crust from the 3D FWI model with

same markings and labels as in a; c) shows the location of these grids within the 3D FWI grid shown in Figure 1 d) thickness of the crystalline crust with fault intersections with the S-reflector in solid black lines. Fault 5.4.1 is plotted as dashed black line to indicate that it does not clearly cut (weak reflection) the S-reflector; e) mean velocity of the crystalline crust. The red arrow shows the north direction. Upper scale bar is for a) and b) and lower scale bar is for c) and d).

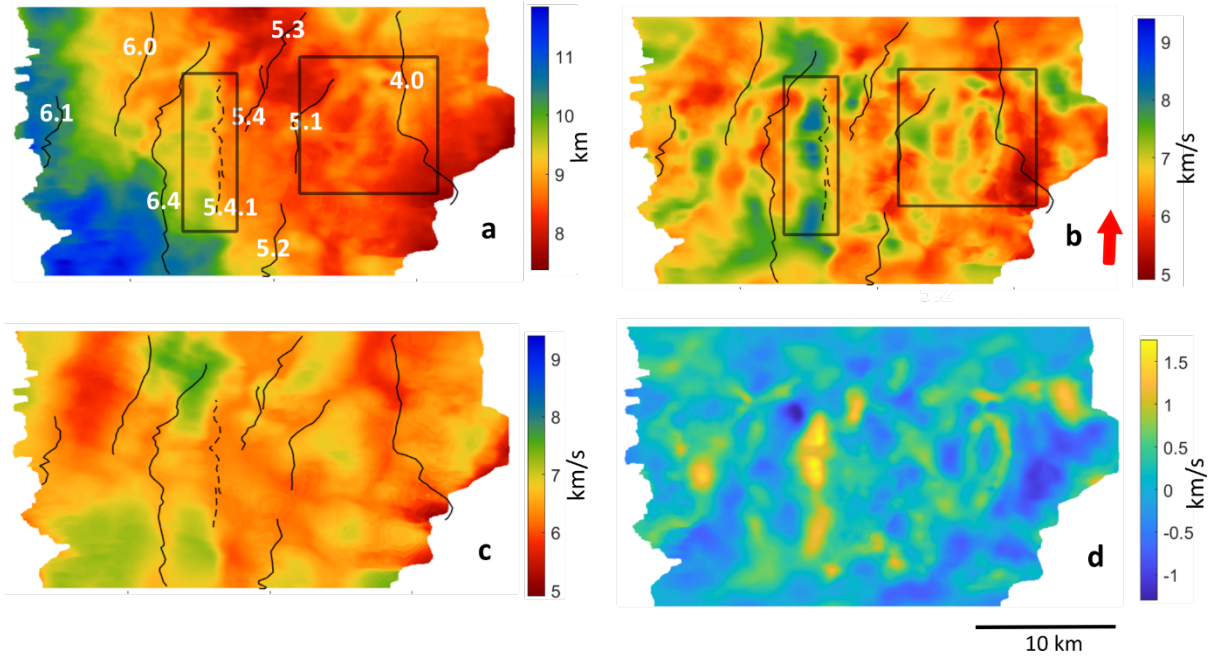

Figure 3 a) S-reflector map converted to depth using the 3D FWI model with fault intersections in solid black lines. Fault 5.4.1 is plotted as dashed black line to indicate that it does not clearly cut (weak reflection) the S-reflector. Solid black rectangles highlight the regions that show good correlation between the shapes on the S surface and the velocity map b; b) velocities at the S-reflector from the 3D FWI model averaged over an interval of 100 m across the S; c) velocities at the S-reflector from the 3D traveltime tomographic model of Bayrakci et al. (2016); d) difference between the 3D FWI and traveltime model at the S-reflector (km/s). The red arrow points to the north; the fault intersection labels in a are same for b and c

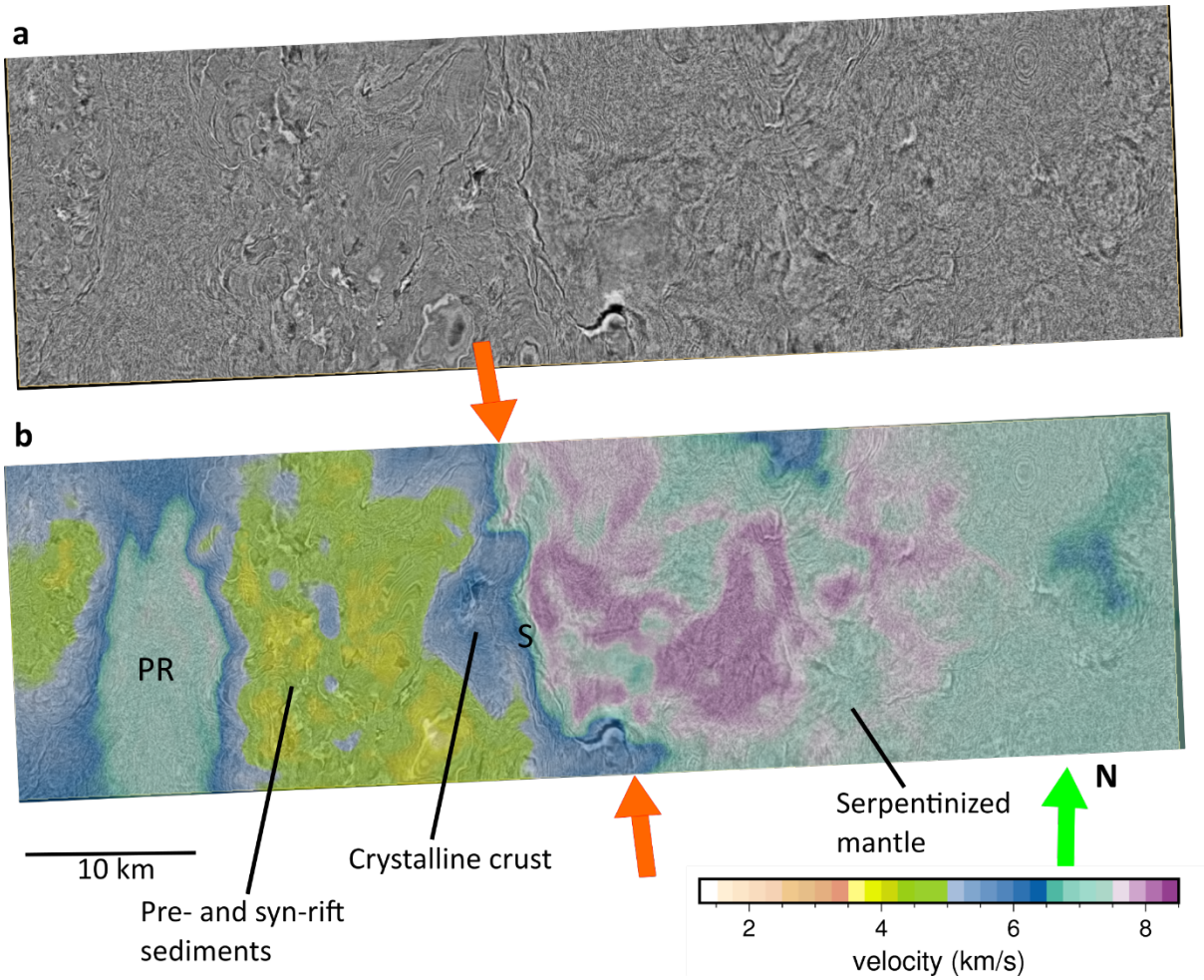

Figure 4 a) Time slice from the 3D multichannel seismic data across the whole surface of the volume (location in Figure 1) at 9 s (average time of the S-reflector) b) 3D FWI model overlaid on the time slice at 9s. The velocity model shows a good match with the reflector (S) at the crust-mantle boundary pointed by the orange arrows. The green arrow marks north. Labels S and PR are the S-reflector and the Peridotite Ridge, respectively.

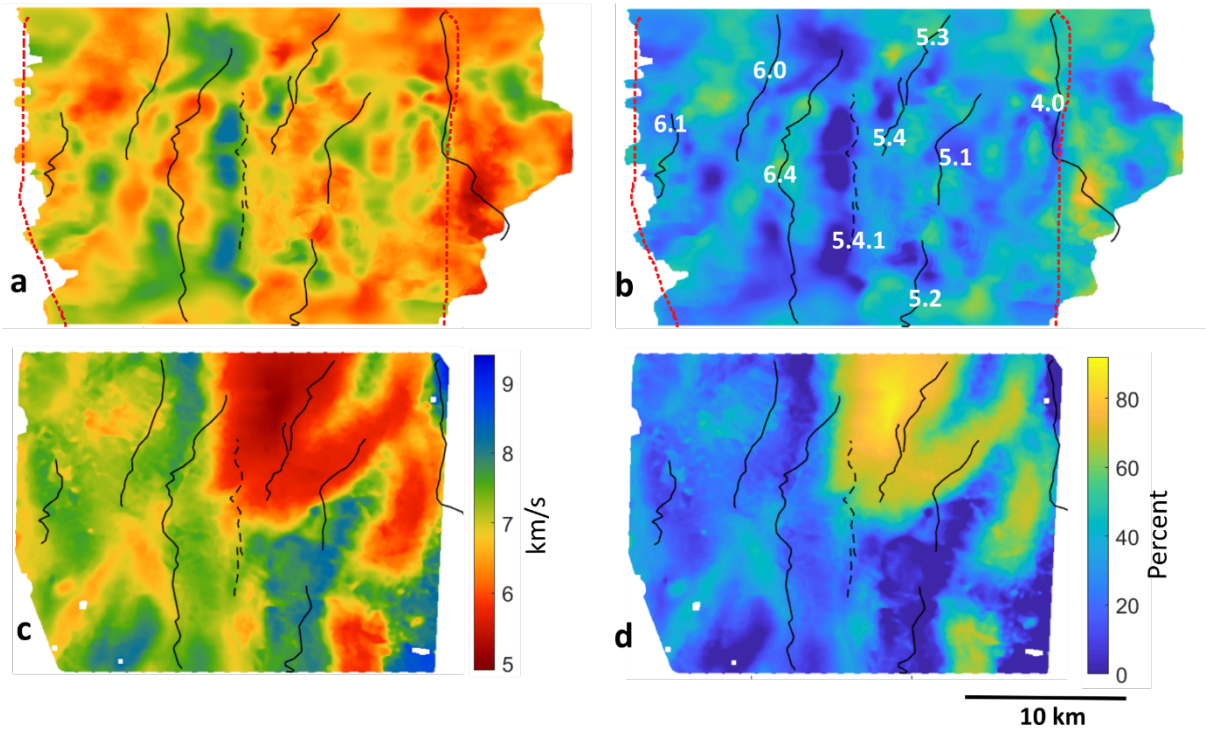

Figure 5 a) Velocities below the S-reflector averaged over a window of 100 ms (~340 m) from the 3D FWI model; b) serpentinization map derived from velocities in a. Black lines indicate the intersections of the faults with the S-reflector and their numbers are indicated in white (numbering after Lymer et al. 2019). Fault 5.4.1 (dashed black line) does not clearly cut the S-reflector. The color scales for a and b are same as c and d, respectively. The red dashed lines in a and b mark the extent of c and d maps; c) velocities immediately below the S-reflector estimated by training a machine learning algorithm (Schuba et al. 2019a); d) percentage map of the serpentinization of the topmost mantle using velocities from c (Schuba et al. 2019b); fault intersections are marked as in Fig. 4. Note that in c) and d) we use the full computed grids, parts of which are masked by Schuba et al. (2019a; b).

We observe very little match between our map of mean velocities over an interval of 100 ms (~340m) below the S-reflector (Figure 5a) and that of Schuba et al. (2019) (Figure 5c). The maximum and minimum velocities in Fig. 5c are ~9.3 km/s and ~4.3 km/s, respectively, while the FWI-derived values are 8.2 km/s and ~5.3 km/s, respectively. The mean and standard deviation of the velocities in Fig. 5c are 6.9 km/s and 0.8 km/s, respectively. These values are higher than the FWI mean velocity and standard deviation of 6.7 km/s and 0.5 km/s, respectively. Using the velocities, we estimated degrees of serpentinization below the S-reflector using a linear relationship between the P-wave velocities and volume percent serpentine in peridotites (Christensen, 2004), as also used by

Schuba et al. (2019b). The degree of serpentinization from the 3D FWI model ranges from 0 to 84%, with a mean of ~34% (Figure 5b), whereas the mean serpentinization in Fig. 5d. is ~32 %. In the central northern region, Schuba et al. (2019b) predict high degrees of serpentinization along the fault intersections 5.3 and 5.4 that are not observed in the serpentinization map from FWI (Figure 5).

Velocity models along profiles close to the OBS locations show a good match with interpretations from the 3D pre-stack time-migrated multichannel seismic volume (Figures 6 and 7; Lymer et al. 2019). The velocities within the sediment column are less reliable than those in the crystalline crust due to the sparse OBS spacing, so are not discussed here.

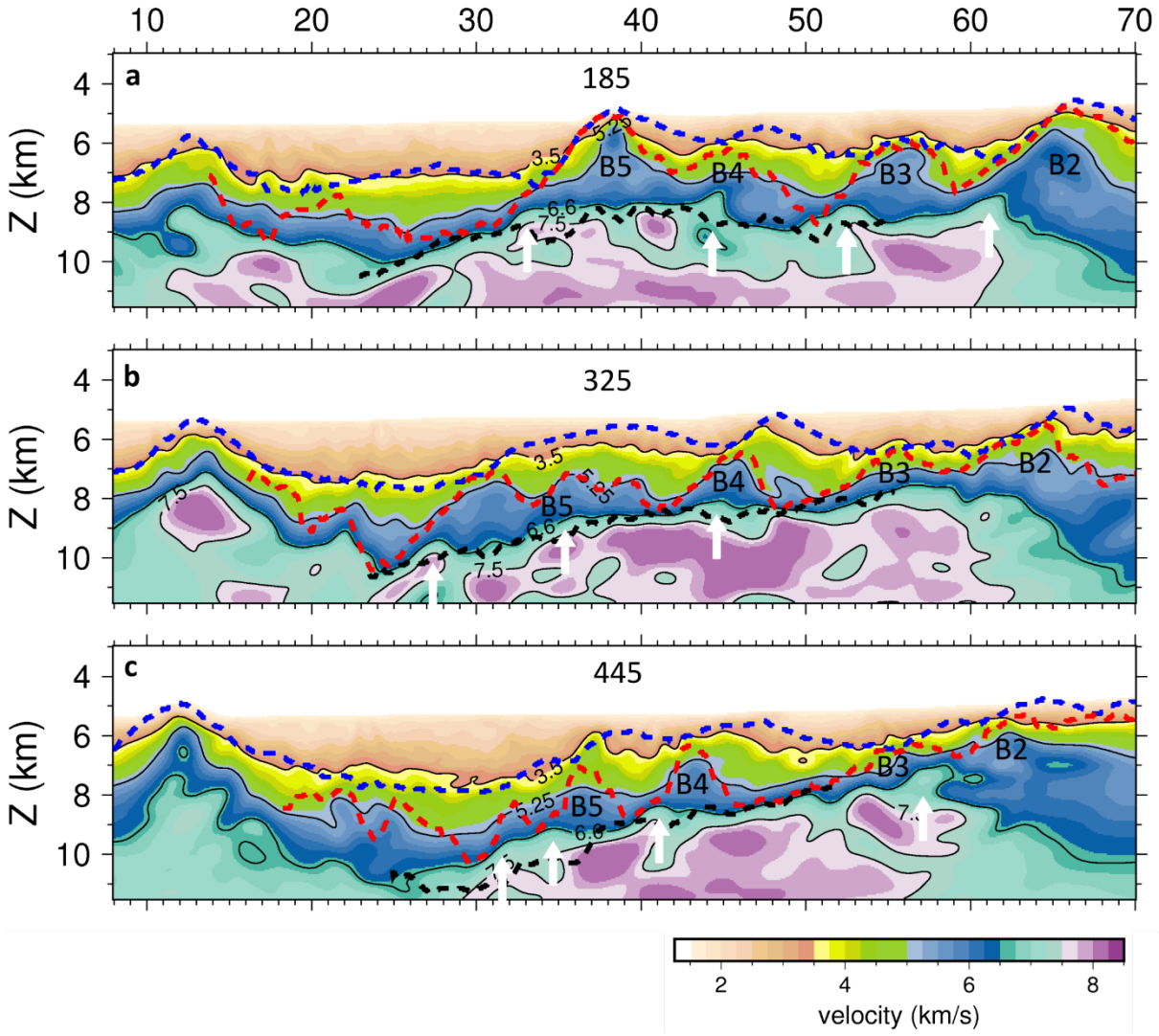

Figure 6 Velocity-depth sections along profiles 185 (a), 325 (b) and 445 (c) overlaid with interpretations from the multichannel seismic volume. See Fig. 1 for locations. Dashed blue line indicates the top of the syn-rift sediment, dashed red line indicates the top of the crystalline crust and dashed black line indicates the S-reflector (Lymer et al. 2019). White arrows point towards shallowing of the 6.6 km/s velocity contour, which marks the top of the lower crust in the GIB (Pérez-Gussinyé et al. 2003) (see text for detail). In profile 325, the 5.25 km/s contour shows a good match with the top of the crystalline crust. Fault block numbers (B-series) are from Lymer et al. (2019).

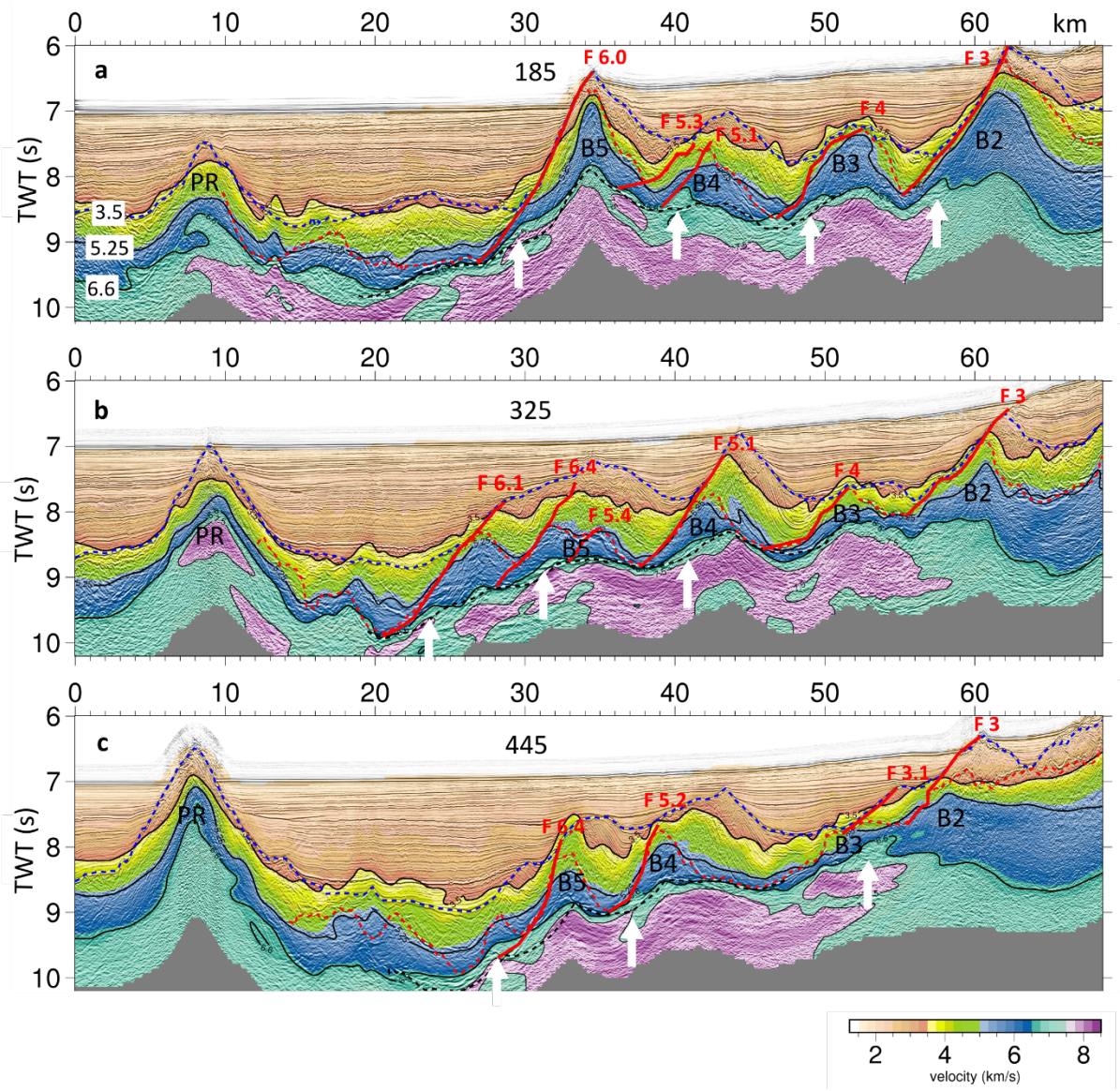

Figure 7 Time-converted velocity sections overlaid on 3D multichannel seismic images along profiles 185 (a), 325 (b) and 445 (c) with interpretations. Dashed blue line indicates the top of the syn-rift sediment, dashed red line indicates the top of the crystalline crust and dashed black line indicates the S-reflector (Lymer et al. 2019). Thick red lines indicate the block bounding faults. White arrows point towards the regions where the velocity contour 6.6 km/s shallows. Velocity contours as solid black lines are as in Figure 6. Fault block are numbers (B-series) from Lymer et al. (2019).

1. Discussion

(a) Nature of the crystalline crust

Here we discuss the nature of the crust in the DGM based on the velocities derived from the 3D FWI and compare our results with the velocity models from other similar tectonic settings. We also present evidence for lower crustal exhumation that may have occurred during the rifting.

In locations where the thickness of the crystalline crust is less than 2 km, the velocity tends to be around 6 km/s and higher, while in the locations where the crust is thicker, the velocity varies between ~4.75 km/s (mean) and the velocity at the S-reflector (~6.7 km/s). The mean velocity of the crystalline crust in the DGM is 6.01 ± 0.44 km/s (Figure 2), which is less than (but within error of) the global velocity average of the continental crust, including velocity models from diverse tectonic settings, of 6.45 ± 0.21 km/s (Christensen & Mooney, 1995). However, the mean velocity is also close to the global means for extended crust (6.05 ± 0.18 km/s) and rifts (6.02 ± 0.14 km/s) at 10 km depth (Christensen & Mooney, 1995), i.e. in the upper crust. These global averages do not include velocity models from hyperextended zones. The velocity limits of the crystalline crust in the DGM agree well with those of thinned continental crust in the northern part of the Southern Iberian Abyssal Plain (SIAP; Figure 1) where the velocity ranges between 5.0 and 6.6 km/s (Chian et al. 1999). This comparison is appropriate because the thickness of the hyper-extended crystalline crust in the SIAP is in the same range (2-5 km) as in the DGM, and the northernmost line of Chian et al. (1999) is only ~170 km from the southern limit of our study area. Another interesting comparison is with crustal velocities in the Galicia Interior Basin (GIB; Figure 1) immediately landward of the DGM, which provide insights into earlier stages of extension of the lithosphere. In the centre of the GIB, the crystalline crust thickness is ~7-8 km, with the upper and lower crust identified as distinct layers (Pérez-Gussinyé et al. 2003). The velocity limits for the upper and lower crust obtained from wide-angle seismic data in the GIB are 5.3-6.4 and 6.6-6.9 km/s, respectively (Pérez-Gussinyé et al. 2003). These limits together encompass the velocity limits of the crystalline crust in the DGM, suggesting that this crust is composed of both upper and lower crustal rocks. In addition, recovery of lower crustal rocks from drilling at the neighbouring SIAP (Whitmarsh et al. 2000) further supports the possibility of presence of both upper and lower crustal rocks in the DGM. Measurements on the lower crustal cores showed velocities between 4.9-6.6 km/s with a modal velocity of ~5.7 km/s (Whitmarsh et al. 2000) which is within the limits of the crustal velocities observed in the DGM.

It is difficult to differentiate crustal and upper mantle rocks using only P-wave seismic velocities because serpentinized upper mantle rocks can show a wide-range of velocities (~5-8.3 km/s for intact rock), depending on the degree of serpentinization, spanning the velocity limits of crystalline crust (Christensen, 2004). Based on seismic images and high-resolution velocity models, the lower regions of the crystalline crust in the vicinity of the S-reflector have been previ-

ously interpreted as fractured and brecciated serpentinized peridotites and/or crustal rocks (Reston et al. 1996). Imaging the S-interval as identified by Leythäuser et al. (2005) and Schuba et al. (2018) is beyond the resolution of our 3D inversion strategy (Boddupalli et al. 2021), so our velocity range and mean include this interval.

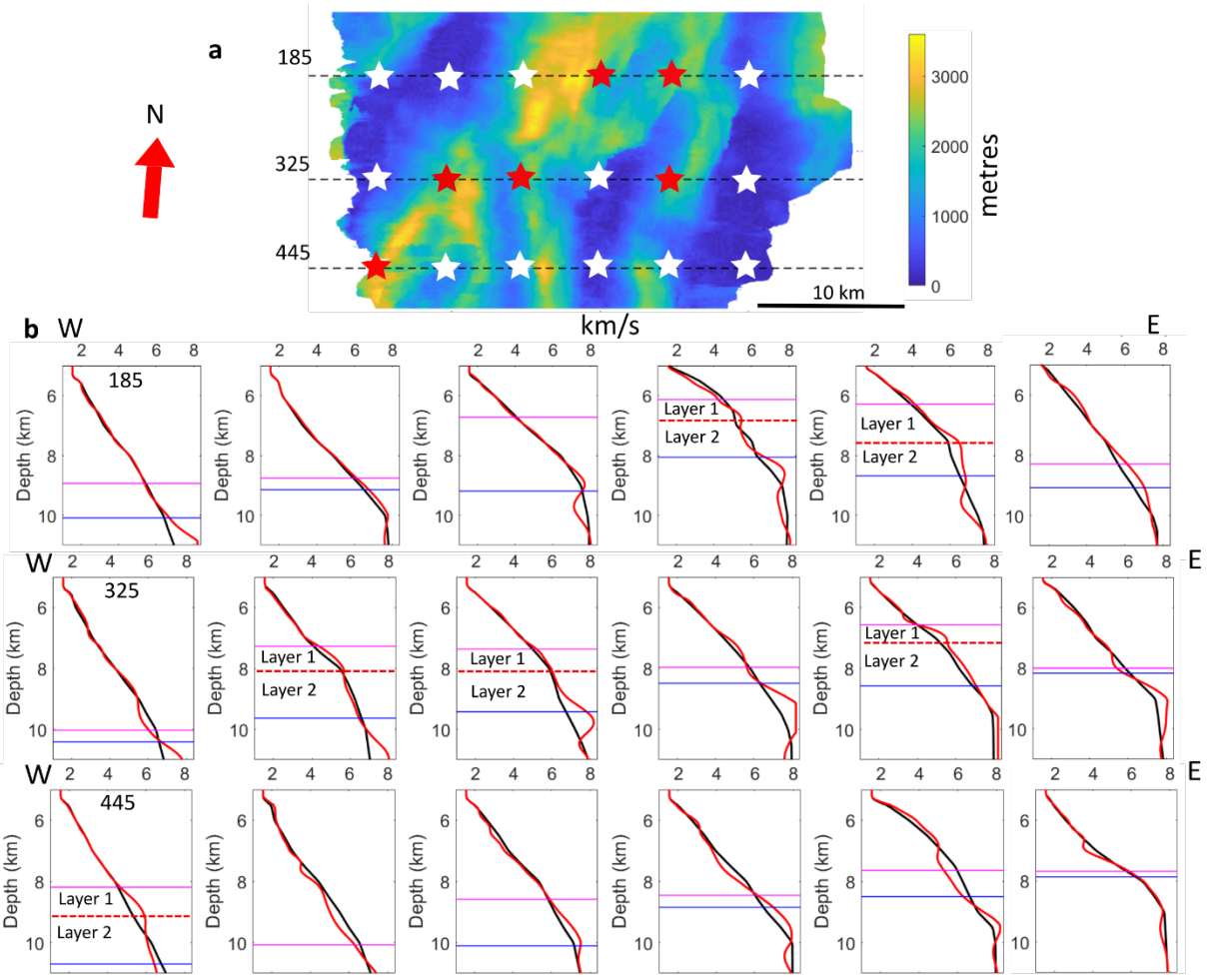

Figure 8 a) Crystalline crustal thickness calculated between the top basement and S surfaces, with white and red stars showing the locations of the 1D velocity profiles extracted from the 3D FWI model along profiles 185, 325 and 445. Red stars indicate the locations where we observe two layers within the crystalline crust; b) 1D velocity profiles from the starting (black) and 3D FWI model (red) with profile location following the same order as the order of the white stars on the profiles. Pink and violet colours in each profile mark the top of the crystalline crust and S-reflector depths, respectively. The dashed red line indicates the boundary between two distinct layers within the crystalline crust.

1. **Two-layered continental crust?**

In a few locations, the crystalline crust can be divided into a higher-gradient upper part and a lower-gradient lower part (Figure 8). To investigate further this subdivision, velocity profiles were plotted every 1 km between 25 and 35 km along profile 325 across one fault block (Figure 9). Here it can be observed that as the crystalline crust thickens, the velocity variation within the crystalline crust appears to split into two layers with different velocity gradients. This layering is only observed where the thickness of the crystalline crust is greater than ~2 km (Figure 8). It is possible that the layering might be present in the locations where the crust is thinner too, but is not resolved in our model. The upper layer (Layer 1 on Figure 9) has a higher velocity gradient (0.2-0.3 s^{-1}) with the velocity ranging between ~4.75 and 5.3 km/s, and the lower layer (Layer 2) shows velocity range between ~5.3 and 6.7 km/s with a lower velocity gradient (Figure 9). The velocity ranges of these layers vary along and across the volume. Layer 1 marks the top of the crystalline crust and its high gradient and low velocities are inferred to result from fracturing and related mechanisms, as in the GIB and the Porcupine basin (Pérez-Gussinyé et al. 2003; Watremez et al. 2018). Layer 1 thickens towards the centre of the fault block number B5 where the crust is thickest (Figure 9), perhaps indicating that the fracturing processes were mainly active over the top of the fault blocks. Moreover, this zone correlates well with a previous interpretation from seismic reflection images that the crests of fault blocks were flattened as a result of mass wasting or subaerial erosion during rifting (Reston et al. 2005; Reston et al. 2007).

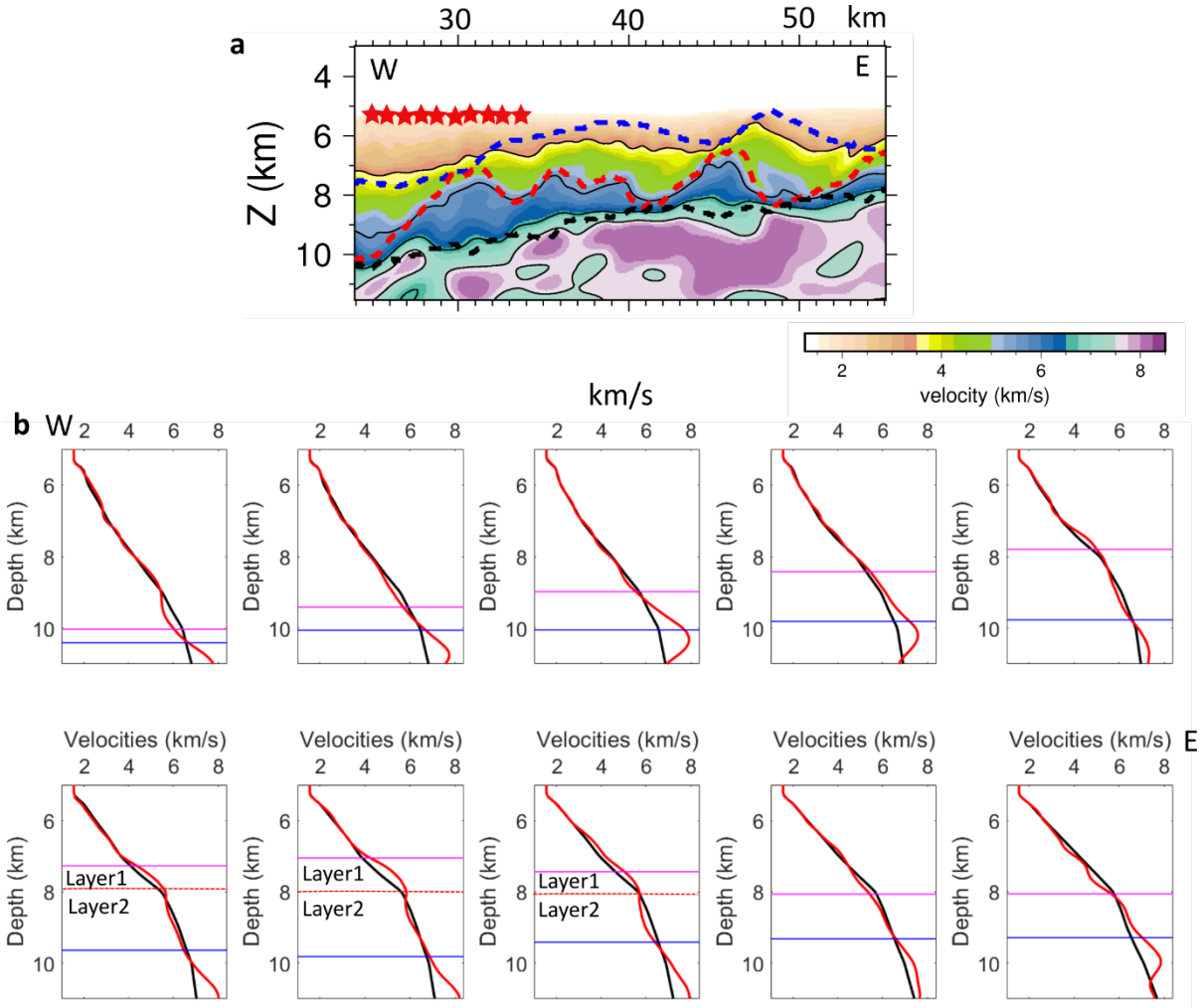

Figure 9 a) Red stars indicate the locations of the 1D velocity profiles shown in (d) between 25 and 35 km (west to east) on the velocity profile 325 with interpretations as in figure 6 c) 1D velocity profiles from the 3D FWI model at the locations indicated by the red stars in (a). As the crustal thickness increases towards block number B5 in the west, the 1D velocity model shows two distinct crustal layers.

1. **Exhumation of the lower crust**

During the late stages of rifting at magma-poor margins, it has been proposed that the upper and lower crust become tightly coupled, with progressive embrittlement of the lower crust (Pérez-Gussinyé & Reston, 2001). Thermo-mechanical modelling predicts that the lower crust is exhumed along an "exhumation channel" under the footwall of the active normal faults and eventually becomes

brittle during the extension (Brune et al. 2014). Hot and weak lower crust because of its ductile nature absorbs the amount of extension accommodated by the normal faults by flowing locally (Brune et al. 2014, 2017). Towards the centre of the GIB, seismic reflection data and a coincident 2D velocity model suggest that normal faults cutting through the brittle upper crust progressively cut into the lower crust, exhuming high-velocity lower crustal rocks within their footwalls to accommodate the fault offsets (Pérez-Gussinyé et al. 2003). However, Reston & McDermott, (2014) explained the presence of higher velocities just below the top basement in the GIB using two phases of faulting which exhumed lower crustal rocks to shallower depths. We observe evidence for the exhumation process in the 3D FWI model of the DGM: if we consider the 6.6 km/s velocity contour as the top of the lower crust from the GIB, it shallows under the footwall of the faults (Figure 6 and 7). Although the undulations on the 6.6 km/s contour in a few locations are small, there are locations where the velocity perturbations rise up to 1 km above the S-reflector beneath the footwall of the normal faults (Figure 6 & 7). It is possible that these high-velocity rocks might be serpentinites, but it is less likely that mantle rocks exhume nearly 1 km above the S-reflector. Additional support that the 6.6 km/s velocity contour ridges beneath the footwall blocks might be lower crustal rocks comes from the Ocean Drilling Program (ODP) data of the SIAP, where lower crustal rocks were cored on top of a basement high (ODP sites 1068 and 900) adjacent to serpentinites seaward (ODP site 1067) separated by a detachment fault, the H-reflector (Krawczyk et al. 1996). In the SIAP, where the hyperextended crust is similar to the DGM, it is suggested that a small lens of the lower crustal rocks at the top of a basement high was exhumed from a deeper depth where a seaward-dipping fault intersects the H-reflector (Whitmarsh et al. 2000). This exhumation occurred along a high-angle, landward-dipping normal fault on the eastern flank of the basement high that offsets the H-reflector (Whitmarsh et al. 2000). This is exactly the same depth range in the DGM where we observe the 6.6 km/s velocity contour shallows beneath the footwall blocks along the normal faults, this correspondence between the SIAP and DGM suggests that the shallowing of the velocity contour might be due to the lower crustal rocks in the DGM. In our velocity model, there is no clear evidence for a separate upper and lower crust within the fault blocks, so we use the 6.6 km/s velocity contour as representative of the lower crust to highlight its deformation during the faulting. If the crust in the DGM has undergone similar initial extension stages as in the GIB, exhumation of the lower crust under the footwalls of the overlying fault blocks would have occurred when it was still ductile, accompanied by cooling and embrittlement. As the extension progressed further into the distal margin, the lower crust beneath the footwall of the faults progressively became brittle and coupled with the upper crust. However, it is also possible that the lower crustal rocks were exhumed during initial phases of faulting assuming faulting in the DGM occurred in multiple phases. Lower crustal exhumation forms a component of all the lithospheric extension mechanisms that are proposed for the final stages of rifting: the polyphase model, sequential faulting, rolling hinge model (Buck, 1988; Lymer et al. 2019; Ranero & Pérez-Gussinyé, 2010; Reston,

2005).

1. **Velocities at and below the S-reflector**

The velocity pattern at the S-reflector shows a good correspondence with the topography of the S-surface (Figure 3). The deep and shallow features correlate with locally high and low velocities, respectively (Figure 3). In the central region, the model shows high velocities (> 8 km/s) indicating the presence of unaltered peridotites there (Figure 3). These high-velocity locations may have higher uncertainties in the velocity due to the significant anisotropy that can be associated with unaltered peridotites (Christensen, 2004), that is not accounted for in our inversion (Boddupalli et al. 2021). In a few locations the velocity reaches 8.2 km/s, which was set as the maximum velocity allowed in the inversion (Boddupalli et al. 2021). However, the anomaly restoration test supports the presence of these high velocities (Supplementary Figure 1).

The 3D FWI result also shows a good match with the multichannel seismic image time slice sections at the mean S-reflector depth (Figure 4). This good match gives confidence in the velocities at this depth, and we infer that the velocity map from the 3D FWI is likely more accurate than the map of Schuba et al. (2019a). Their machine learning approach can have pitfalls that are difficult to address. We suspect that the observed differences between the two maps are primarily due to the limited dataset used for training the algorithm and limitations of the machine learning method. Boddupalli et al. (2021) demonstrated that the 2D FWI result, which was used to train the machine learning, did not fully resolve the velocities below the S. An additional issue is the probable presence of wider velocity variations within the whole 3D volume than were present in the training dataset.

1. **Serpentinization map of the DGM**

The map of Schuba et al. (2019b) shows a match between the orientation of the crustal blocks and the alignment of the serpentinized areas (Figure 2d; 5c&d). We observe an overall alignment between the fault intersections and serpentinized areas in our FWI serpentinization map, but this alignment is less tight (Figures 2 & 3). The machine learning serpentinization map (Figure 5d) shows a noticeable correlation between the crystalline crustal thickness (Figure 2d) and serpentinization patterns (Figure 5d). The regions with higher serpentinization values have thicker crust, and where the crust is thinner, low serpentinization is predicted. Since serpentinization is mostly controlled by the water supply to the mantle (Emmanuel & Berkowitz, 2006; Macdonald & Fyfe, 1985), one would expect an inverse correlation between crustal thickness and serpentinization as thicker crust can impede the water flow to the mantle compared too thinner crust. Therefore, we suspect that the observed correlation might be a biased prediction of the machine learning algorithm because crustal thickness is one of the inputs into the algorithm (Schuba et al. 2019).

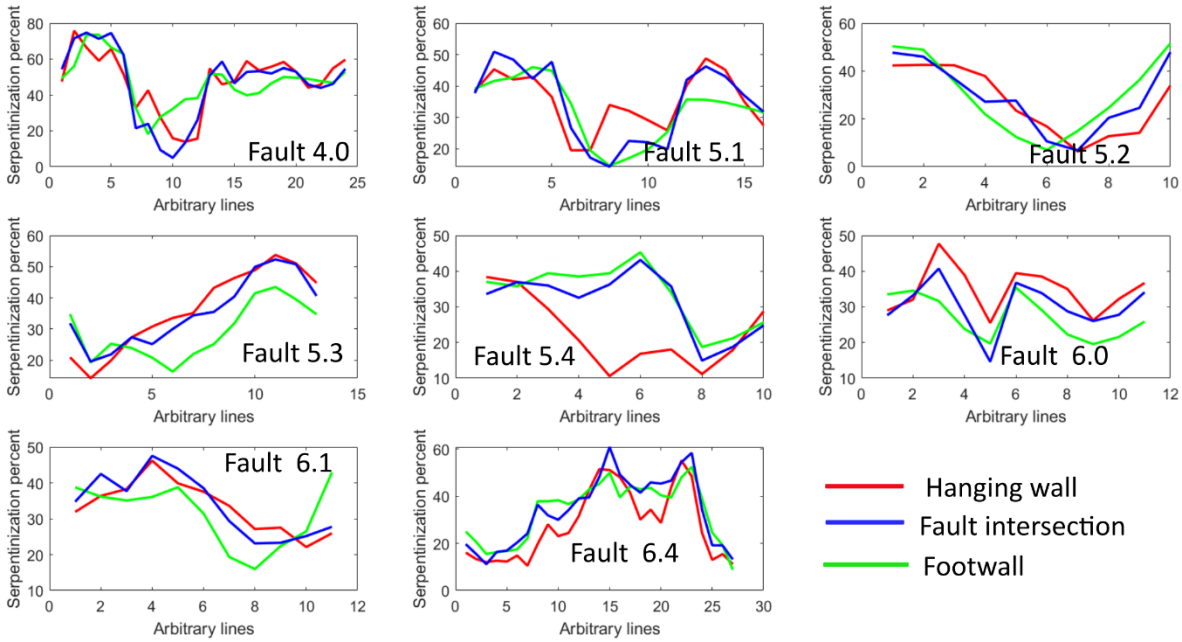

Figure 10 Serpentinization estimates averaged over a length of 1 km along the arbitrary lines from the point of fault intersection (blue) in the hanging wall (red) and footwall (green) directions for each fault intersection. The x-axis represents number of arbitrary lines intersected by fault intersections from south to north.

The overall alignment between the edges of serpentinized areas and overlying normal faults indicates that these faults played an important role in transporting water to the mantle (Figure 5b). To further investigate the variation in the serpentinization across the fault intersections, we plotted mean serpentinization under the footwall at the fault intersection and under the hanging wall for each fault intersection over a length of 2 km around the fault intersections (1 km on either side of the fault intersection) along a series of arbitrary lines (Supplementary Figure 3) in the direction of the corrugations observed in the 3D reflection volume as defined by Lymer et al. (2019) (Figure 10). Most of the faults show higher serpentinization values under hanging wall side than footwall side across major part of their intersection with the S (Figure 10). However, at fault intersections 5.4 and 6.4, low serpentinization occurs toward the hanging wall side. These anomalies may be due to changes in the water supply along the faults affected by tectonics and other factors. Intriguingly, in the central region, the alignment of the fault intersection 5.4.1 on the eastern edge an area of limited serpentinization (Figure 5b) suggests that little or no water reached the mantle along this fault. Moreover, fault 5.4.1 does not show clear reflections reaching the S-reflector on the vertical sections of the 3D seismic volume, e.g. between 30 and 40 km along profile 325 (Supplementary Figure 4). These

observations add strong support to the hypothesis that the overlying normal faults played a key role in transporting water to the mantle and serpentinizing it. The observed good alignment between the faults and areas of serpentinization (Figure 5) partly supports a post-rift serpentinization phase in which water was transported along the faults after the fault movement stopped until the faults were sealed. However, it does not explain the patterns that do not show proper alignment. These non-aligned patterns of serpentinization can be attributed to a syn-rift serpentinization phase that was influenced by the rift tectonics and was then partially overwritten by post-tectonic serpentinization. This continuous serpentinization mechanism can explain the inferred aligned and non-aligned serpentinization patterns (Figure 5b).

Bayrakci et al. (2016) established a strong positive correlation between the average fault heaves for individual faults and degree of serpentinization beneath the hanging wall. However, that study only used fault interpretations along three 2D seismic profiles from the DGM. We have revisited this correlation using the fault heaves obtained from the 3D seismic volume (Lymer et al. 2019). Our approach for establishing a correlation between fault heaves and degree of serpentinization differs from that of Bayrakci et al. (2016) in which the degree of serpentinization was averaged over a window of 7 km laterally and 2.5 km vertically below S along 2D seismic lines for each normal fault intersecting the S. In this study, we calculated average degree of serpentinization related to each normal fault from the serpentinization map (Figure 5b) by averaging the degree of serpentinization within 1 km along the arbitrary lines and along the faults intersection with S (Figure 10; Supplementary figure 3). The FWI serpentinization map is averaged over 100 ms vertically and we calculated average degree of serpentinization for each fault on either side of the fault intersection (hanging wall and footwall sides, Figure 11). Therefore, our average serpentinization values for each fault are averaged 100 ms vertically, 1 km along the arbitrary lines on the hanging wall and footwall sides of each fault intersection, and along the fault intersections (Figure 5b; Supplementary figure 3). In contrast to Bayrakci et al. (2016), we find a weak correlation between the mean fault heaves and degree of serpentinization predicted below the hanging wall (Figure 11). It is possible that since our approach included more data points from the complete 3D seismic volume (Lymer et al. 2019) into the fit than Bayrakci et al. (2016) and estimated serpentinization in the direction of extension using a high resolution velocity model (Boddupalli et al. 2021), has highlighted the contribution of additional processes of transport of water that affected the water transportation process to the mantle during hyper-extension, resulting in a weak correlation between heaves and percentage of serpentinization (Figure 11). Processes that can be invoked are unrecognized polyphase faulting (McDermott & Reston, 2015; Reston, 2005) and crosscut between fault generations during the development of S (Reston et al. 2007; Lymer et al. 2019), resulting in complex faulting patterns that would logically complicate and weaken the correlation between the serpentinization patterns and the fault heaves of the current block bounding faults that form the S-surface.

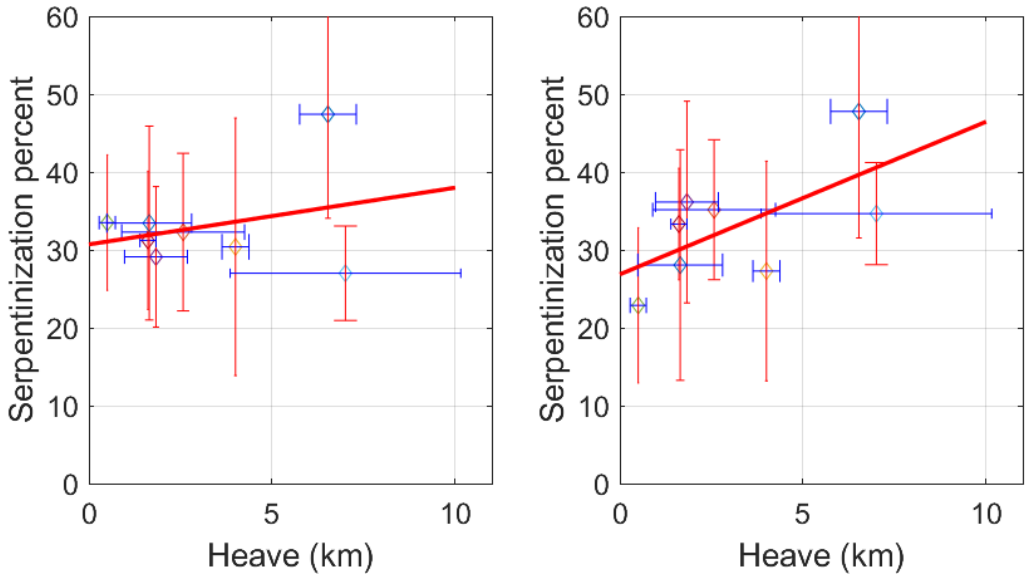

Figure 11 Correlation plot between the average fault heave and serpentinization percent under footwall (left; R-square: 0.08) and hanging wall blocks (right; R-square: 0.2). The diamonds represent each fault plotted at their average heave and serpentinization values. The error bars on the diamonds indicate one standard deviation. The red solid lines represent a linear fit between the points.

The pattern of serpentinization shows a correlation with the topography of the S-reflector with deeper features showing lower serpentinization locally (Figure 5). These localized high and low relief features on the S-reflector may be attributed at least in part to the change in volume resulting from serpentinization (Graham, 1917), especially given the heterogeneous serpentinization pattern (Figure 5). Serpentinization can increase the volume of the rocks by ~40 %, and such a large increase could result in changes in the structure of a bounding surface due to buoyancy (Germanovich et al. 2012; Lister, 1974). Therefore, given the thin overburden, the serpentinization process has affected the topography of the S-surface by causing the expansion of the rocks upward. This correlation is also consistent with our attribution of the velocity reduction in the uppermost mantle primarily to serpentinization, and inconsistent with the idea that the velocity reduction is due to residual fracture porosity (Korenaga, 2017). However, this uplift is not transmitted through the crust as there is no correlation between the depth of S and the top of the crystalline crust (Figure 2a and 3a; Lymer et al. 2019). This lack of correlation supports the idea that serpentinization began after the faults broke through the thinned crust and reached the mantle.

1. Conclusions

We have presented a 3D FWI model along three profiles 185, 325 and 445 ori-

ented in the East-West direction and discussed the nature of the hyperextended crust and exhumation of the lower crust during the late stages of extension at the DGM. We have explored variations in velocity at the top of the crystalline crust, the S-reflector and in the mantle at 100 ms depth below the S-reflector. Based on our results, we conclude the following:

1. The mean velocity of the crystalline crust in the DGM (~ 6 km/s) matches closely global averages for extended continental crust at a depth of 10 km. The velocities in the crystalline crust vary between ~4.75 and 6.7 km/s, matching closely those observed in the neighbouring SIAP and GIB. Within the crystalline crust, we find limited evidence for distinct upper and lower crustal layers.

2. At the top of the crystalline crust a layer with a high velocity gradient is identified where the crystalline crust thickness is greater than 2 km, that we attribute to fracturing and related mechanisms at the top of the crystalline crust.

3. The 6.6 km/s velocity contour shallows under the footwall of the overlying normal faults, consistent with exhumation of the lower crust under the footwall of the normal faults to accommodate extension by ductile flow along the normal faults during early extension phases.

4. A good match between the velocity variations just below the S-reflector and the topography of S may be attributed to variable buoyancy of serpentinite, consistent with serpentinization being the primary cause of these velocity variations in the upper mantle.

5. An overall alignment between the fault intersections and edges of regions of serpentinization patterns suggest that water transportation to the mantle continued after fault activity ceased and resulted in partial overprinting of the initial serpentinized areas developed during rifting.

6. We find a weak correlation between the fault heaves and the degree of serpentinization beneath the hanging-walls of faults and no correlation beneath the footwalls, indicating that serpentinization was controlled by a complex unrecognized faulting during rifting.

1. **Data Availability**

The multichannel seismic data set used for this study can be found online (https://doi.org/10.1594/IEDA/500151). The OBS data underlying this paper are being uploaded to https://ww w.pangaea.de. Prior to availability there, they will be shared on a reasonable request to the corresponding author.

1. **Acknowledgements**

Data acquisition was supported by the U.S. National Science Foundation (grant OCE-257 1031769), the UK Natural Environment Research Council (NERC; grant NE/E016502/1 and NE/E015883/1), and GEOMAR. Ocean bottom instrumentation was provided by the NERC UK Ocean Bottom Instrumentation

Facility (Minshull et al. 2005) and by GEOMAR. We thank Joanna Morgan, Imperial College London, for assisting us with 3D full waveform inversion. We acknowledge the use of the IRIDIS High Performance Computing Facility, and associated support services at the University of Southampton, in the completion of this work. The 3-D ProMAX/SeisSpace package, supplied by Halliburton under a university software grant, was used to preprocess and analyse the field data within University of Southampton.

References

Bayrakci, G., Minshull, T. A., Sawyer, D. S., Reston, T. J., Klaeschen, D., Papenberg, C., et al. (2016). Fault-controlled hydration of the upper mantle during continental rifting. *Nature Geoscience*, *9*(5), 384–388. https://doi.org/10.1038/ngeo2671Boddupalli, B., Minshull, T. A., Morgan, J., Bayrakci, G., & Klaeschen, D. (2021). Comparison of two- and three-dimensional full waveform inversion imaging using wide-angle seismic data from the Deep Galicia Margin. *Geophysical Journal International*. https://doi.org/10.1093/gji/ggab164Boillot, G., & Winterer, E. L. (1988). *DRILLING ON THE GALICIA MARGIN: RETROSPECT AND PROSPECT*. *Proceedings of the Ocean Drilling Program, Scientific Results*.Brune, S., Heine, C., Pérez-Gussinyé, M., & Sobolev, S. V. (2014). Rift migration explains continental margin asymmetry and crustal hyper-extension. *Nature Communications*, *5*, 1–9. https://doi.org/10.1038/ncomms5014Brune, S., Heine, C., Clift, P. D., & Pérez-Gussinyé, M. (2017). Rifted margin architecture and crustal rheology: Reviewing Iberia-Newfoundland, Central South Atlantic, and South China Sea. *Marine and Petroleum Geology*, *79*, 257–281. https://doi.org/10.1016/j.marpetgeo.2016.10.018Buck, W. R. (1988). Flexural Rotation of Normal Faults, *7*(5), 959–973.Carlson, R. L., & Miller, D. J. (2003). Mantle wedge water contents estimated from seismic velocities in partially serpentinized peridotites. *Geophysical Research Letters*, *30*(5), n/a-n/a. https://doi.org/10.1029/2002gl016600De Charpal, O., Guennoc, P., Montadert, L., & Roberts, D. G. (1978). Rifting, crustal attenuation and subsidence in the Bay of Biscay. *Nature*, *275*(5682), 706–711. https://doi.org/10.1038/275706a0Chian, D., Louden, K. E., Minshull, T. A., & Whitmarsh, R. B. (1999). Deep structure of the ocean-continent transition in the southern Iberia Abyssal Plain from seismic refraction profiles: Ocean Drilling Program (Legs 149 and 173) transect. *Journal of Geophysical Research: Solid Earth*, *104*(B4), 7443–7462. https://doi.org/10.1029/1999jb900004Christensen, N. I., & Mooney, W. D. (1995). Seismic velocity structure and composition of the continental crust: a global view. *Journal of Geophysical Research*, *100*(B6), 9761–9788. https://doi.org/10.1029/95JB00259Christensen, Nikolas I. (2004). Serpentinites, peridotites, and seismology. *International Geology Review*, *46*(9), 795–816. https://doi.org/10.2747/0020-6814.46.9.795Dapeng Zhao, Hasegawa, A., & Horiuchi, S. (1992). Tomographic imaging of P and S wave velocity structure beneath northeastern Japan. *Journal of Geophysical Research*, *97*(B13). https://doi.org/10.1029/92jb00603Davis, M., &

Kusznir, N. (2004). Depth-Dependent Lithospheric Stretching at Rifted Continental Margins. *Proceedings of NSF Rifted Margins Theoretical Institute*. https://doi.org/10.7312/karn12738-005Emmanuel, S., & Berkowitz, B. (2006). Suppression and stimulation of seafloor hydrothermal convection by exothermic mineral hydration. *Earth and Planetary Science Letters*, *243*(3–4), 657–668. https://doi.org/10.1016/j.epsl.2006.01.028Franke, D. (2013, May). Rifting, lithosphere breakup and volcanism: Comparison of magma-poor and volcanic rifted margins. *Marine and Petroleum Geology*. https://doi.org/10.1016/j.marpetgeo.2012.11.003Germanovich, L. N., Genc, G., Lowell, R. P., & Rona, P. A. (2012). Deformation and surface uplift associated with serpentinization at mid-ocean ridges and subduction zones. *Journal of Geophysical Research: Solid Earth*, *117*(7), 1–23. https://doi.org/10.1029/2012JB009372Graham, R. P. . (1917). Origin of massive serpentine and chrysotile asbestos, Black Lake-Thetford area, Quebec. *Economic Geology*, *12*(2), 154–202.Korenaga, J. (2017). On the extent of mantle hydration caused by plate bending. *Earth and Planetary Science Letters*, *457*, 1–9.Krawczyk, C., Reston, T., Beslier, M., & Boillot, G. (1996). 38. Evidence for detachment tectonics on the Iberia Abyssal Plain rifted margin. *Proceedings-Ocean Drilling Program Scientific Results*, 3–26.Leythaeuser, T., Reston, T. J., & Minshull, T. A. (2005). Waveform inversion of the S reflector west of Spain: Fine structure of a detachment fault. *Geophysical Research Letters*. https://doi.org/10.1029/2005GL024026Lister, C. R. . (1974). On the penetration of water into hot rock. *Geophysical Journal International*, *39*, 465–509.Lymer, G., Cresswell, D. J. F., Reston, T. J., Bull, J. M., Sawyer, D. S., Morgan, J. K., et al. (2019). 3D development of detachment faulting during continental breakup. *Earth and Planetary Science Letters*, *515*, 90–99. https://doi.org/10.1016/j.epsl.2019.03.018Macdonald, A. H., & Fyfe, W. S. (1985). Rate of serpentinization in seafloor environments. *Tectonophysics*, *116*(1–2), 123–135. https://doi.org/10.1016/0040-1951(85)90225-2Minshull, T. A., Sinha, M. C., & Peirce, C. (2005). Multi-disciplinary, sub-seabed geophysical imaging. *Sea Technology*, *46*(10).Pérez-Gussinyé, M., Ranero, C. R., Reston, T. J., & Sawyer, D. (2003). Mechanisms of extension at nonvolcanic margins: Evidence from the Galicia interior basin, west of Iberia. *Journal of Geophysical Research: Solid Earth*, *108*(B5), 1–19. https://doi.org/10.1029/2001JB000901Pérez-Gussinyé, Marta, & Reston, T. J. (2001). Rheological evolution during extension at nonvolcanic rifted margins: Onset of serpentinization and development of detachments leading to continental breakup. *Journal of Geophysical Research: Solid Earth*, *106*(B3), 3961–3975. https://doi.org/10.1029/2000jb900325Peron-Pinvidic, G., Manatschal, G., & Osmundsen, P. T. (2013). Structural comparison of archetypal Atlantic rifted margins: A review of observations and concepts. *Marine and Petroleum Geology*, *43*, 21–47. https://doi.org/10.1016/j.marpetgeo.2013.02.002Ranero, C. R., & Pérez-Gussinyé, M. (2010). Sequential faulting explains the asymmetry and extension discrepancy of conjugate margins. *Nature*, *468*(7321), 294–299. https://doi.org/10.1038/nature09520Reston, T., & Mcdermott, K. (2014). An assessment of the cause of the "extension discrepancy" with reference to the west

Galicia margin. *Basin Research*. https://doi.org/10.1111/bre.12042Reston, T. J. (2005). Polyphase faulting during the development of the west Galicia rifted margin. *Earth and Planetary Science Letters*, *237*(3–4), 561–576. https://doi.org/10.1016/j.epsl.2005.06.019Reston, T. J. (2007). The formation of non-volcanic rifted margins by the progressive extension of the lithosphere: the example of the West Iberian margin. *Geological Society, London, Special Publications*, *282*(1), 77–110. https://doi.org/10.1144/SP282.5Reston, T. J., & Mcdermott, K. (2014). An assessment of the cause of the "extension discrepancy" with reference to the west Galicia margin. *Basin Research*, *26*(1). https://doi.org/10.1111/bre.12042Reston, T. J., Krawczyk, C. M., & Klaeschen, D. (1996). The S reflector west of Galicia (Spain): Evidence from prestack depth migration for detachment faulting during continental breakup. *Journal of Geophysical Research: Solid Earth*, *101*(B4), 8075–8091. https://doi.org/10.1029/95JB03466Reston, T. J., Booth-Rea, G., Leythaeuser, T., Sawyer, D., Klaeschen, D., & Long, C. (2007). Movement along a low-angle normal fault: The S reflector west of Spain. *Geochemistry, Geophysics, Geosystems*, *8*(6), 1–14. https://doi.org/10.1029/2006GC001437Schuba, C. N., Gray, G. G., Morgan, J. K., Schuba, J. P., & Sawyer, D. S. (2019). Origin of Serpentinization Patterns Beneath the S-Reflector Detachment Fault in the Galicia Margin, Offshore Spain. *Geochemistry, Geophysics, Geosystems*, *20*(8), 3971–3984. https://doi.org/10.1029/2019GC008400Schuba, C. Nur, Schuba, J. P., Gray, G. G., & Davy, R. G. (2019). Interface-targeted seismic velocity estimation using machine learning. *Geophysical Journal International*, *218*(1), 45–56. https://doi.org/10.1093/gji/ggz142Schuba, C Nur, Gray, G. G., Morgan, J. K., Sawyer, D. S., Shillington, D. J., Reston, T. J., et al. (2018). A low-angle detachment fault revealed: Three-dimensional images of the S-reflector fault zone along the Galicia passive margin. *Earth and Planetary Science Letters*, *492*, 232–238. https://doi.org/10.1016/j.epsl.2018.04.012Sibuet, J.-C. (1992). New constraints on the formation of the non-volcanic continental Galicia-Flemish Cap conjugate margins. *Journal of the Geological Society*, *149*(5), 829–840. https://doi.org/10.1144/gsjgs.149.5.0829Watremez, L., Prada, M., Minshull, T., O'Reilly, B., Chen, C., Reston, T., et al. (2018). Deep structure of the Porcupine Basin from wide-angle seismic data. *Petroleum Geology Conference Proceedings*, *8*(1), 199–209. https://doi.org/10.1144/PGC8.26Whitmarsh, R. B., Dean, S. M., Minshull, T. A., & Tompkins, M. (2000). Tectonic implications of exposure of lower continental crust beneath the Iberia Abyssal Plain, Northeast Atlantic Ocean: Geophysical evidence. *Tectonics*, *19*(5), 919–942.Whitmarsh, R. B., Manatschal, G., & Minshull, T. A. (2001). Evolution of magma-poor continental margins from rifting to seafloor spreading. *Nature*, *413*(6852), 150–154. https://doi.org/10.1038/35093085